Coupled reaction channel analysis of elastic, inelastic, transfer, and fusion cross sections for $^{12}C+^{208}Pb$

S. Santra, P. Singh, S. Kailas, A. Chatterjee, A. Shrivastava, and K. Mahata
Nuclear Physics Division, Bhabha Atomic Research Centre, Mumbai 400 085, India
(Received 22 February 2001; published 25 June 2001)

Elastic, inelastic, and transfer angular distributions were measured for $^{12}C+^{208}Pb$ in the energy range from 58.9 to 84.9 MeV. While the fission fragment angular distributions were measured over the energy range from 58.9 to 79 MeV, the residue cross sections after $2n$ evaporation from the compound nucleus (^{220}Ra) were measured by α counting at 58.9, 60.9, and 62.9 MeV. Combining the above data with the ones from the literature, the fusion cross sections have been obtained. Quasielastic excitation function at 170° was also measured to obtain the fusion barrier distribution. Optical model analysis of the elastic scattering data, using both phenomenological and microscopic models, brought out the pronounced energy dependence of the optical potential at near barrier energies. A simultaneous description of the elastic and all the nonelastic channels was obtained from the coupled reaction channel (CRC) calculations using a consistent set of parameters at all the energies. The effective nucleus-nucleus real potential, obtained from CRC calculations, explained the observed energy dependence of the real part of the optical potential. Thus, the real potential used in these calculations with such a large number of constraints can be considered as the bare nucleus-nucleus potential.

DOI: 10.1103/PhysRevC.64.024602 PACS number(s): 25.70.Jj, 25.70.Bc, 25.70.Hi

I. INTRODUCTION

The energy dependence of the interaction potential between two nuclei solely depends on their structure and the kinetic energy of the projectile. The coupling of the relative motion of two interacting nuclei to their intrinsic degrees of freedom, e.g., rotation, surface vibrations, etc., gives rise to different effective potentials at different beam energies, which in turn generate a distribution in energy of effective potential barriers [1]. The effective potential determined from the optical model analysis of the elastic scattering data exhibits a variation near the Coulomb barrier that has been interpreted in terms of energy dependent polarization potential contributions arising from reaction channel couplings. Its interpretation relies on the already known existence, on the basis of the causality principle, of a dispersion relation connecting the real and the imaginary parts of the potential [2]. Explanation of these optical potentials, by explicit coupled reaction channel (CRC) calculations using correct structure information of all possible reaction channels, and understanding both the dynamics and the mechanism of the nuclear reactions, is of current interest. Ambiguity in assuming the bare potential in the CRC calculations often leads to incorrect conclusions regarding nuclear structure and the reaction mechanism. Restricting the fit to only elastic or elastic and inelastic scattering data with limited range of energy and angular distributions are the primary reasons for these parameter ambiguities. A simultaneous description of elastic, inelastic, transfer, and fusion cross sections over a wide range of energy and angular distributions through the CRC calculations, will essentially be able to fix the unique potential parameters, and is a challenging task.

The motivation of this work was to measure elastic, inelastic, transfer, fission, and ER cross sections for $^{12}C+^{208}Pb$, and study the dynamics of the nucleus-nucleus interaction by a simultaneous explanation of the elastic and all the dominant nonelastic channels, by CRC calculations. Systematic analysis of elastic, inelastic, transfer, and fusion cross sections for $^{12}C+^{209}Bi$ have been reported previously [3], similar to the present investigation, though not as extensive. It is of interest to see the effect of the extra proton in the target (if any) on the interaction potential of the latter system compared to the present case.

The elastic scattering angular distributions for $^{12}C+^{208}Pb$ system have been measured at several energies in the range of 58.9–84.9 MeV. The data are presented in Sec. II. Optical model analysis using both phenomenological and microscopic potentials, has been performed (Sec. III) to find the energy dependent potentials that are explained by the dispersion relation. Section IV deals with the measurement of fission, and ER data. The results of the statistical model and CRC calculations are compared with the data. Measured angular distributions corresponding to the elastic, inelastic, one-neutron and one-proton transfer cross sections along with the fusion cross sections are compared with the CRC results at two near barrier energies ($E_{lab}=62.9$ and 64.9 MeV), and one much above the barrier energy ($E_{lab}=84.9$ MeV) in Sec. V. The quasielastic (QE) excitation functions at 170° are also measured and the barrier distributions (BD) are obtained from the derivative of "$-\sigma_{QE}/\sigma_{Ruth}$" (the ratio of quasielastic to Rutherford scattering) with respect to energy. These results are discussed in Sec. VI. Finally, in Sec. VII, the present results are compared with those for $^{12}C+^{209}Bi$ [3], to look at the effect of the extra proton in the target of the latter system.

II. MEASUREMENTS OF ELASTIC, INELASTIC, AND TRANSFER CROSS SECTIONS

The elastic scattering measurements were carried out using ^{12}C beam at energies $E_{lab}=58.9$, 60.9, 62.9, 64.9, 69.9, 74.9, and 84.9 MeV, from the BARC-TIFR 14UD Pelletron at Mumbai. The targets used were prepared by vacuum

evaporation of ^{208}Pb (of thickness ≈ 250 μg/cm^2) on to a ^{12}C backing (of thickness ≈ 40 μg/cm^2). Three telescopes ($\Delta E - E$) of silicon surface barrier (SSB) detectors were set up inside a 1 m diameter scattering chamber for measuring the projectilelike particles. A monitor (single SSB) detector was mounted at 20° with respect to beam direction for normalization. A second monitor at 25° was mounted on the wall of the scattering chamber. The angular distributions were measured in the range $\theta_{\rm lab} = 20° - 173°$. The angular resolution was about 0.5°. The detector thicknesses were typically 20 to 45 μm for ΔE and 300 to 2000 μm for E detectors. Proper gain matching in ΔE and E signals led to a total energy resolution of $\simeq 500$ keV. It was possible to identify charge and mass separated reaction products from ^{1}H to ^{14}C in the two-dimensional spectrum of ΔE vs $E + \Delta E$ obtained from a fast-slow coincidence set up. While the separation between the elastic and the inelastic populating the 1st excited state of ^{208}Pb (3^-,2.62 MeV) is good, the inelastic states 2^+ (4.2 MeV) of ^{208}Pb and 2^+ (4.44 MeV) of ^{12}C are merged together. For one neutron pickup (^{13}C) channel, the ground state peak corresponds to ^{13}C (g.s., $1p_{1/2}$)$\otimes$ ^{207}Pb (g.s.,$3p_{1/2}$) of ^{208}Pb(^{12}C,^{13}C)^{207}Pb reaction. The second peak corresponds to ^{13}C(g.s.,$1p_{1/2}$)$\otimes$ [^{207}Pb (0.59 MeV,$2f_{7/2}$) plus ^{207}Pb (0.90 MeV,$3p_{3/2}$)]. The combined cross sections have been extracted for these two channels as the two peaks were not energetically well separated. In case of one proton stripping channel (^{11}B), the three states corresponding to the ground state ($1p_{3/2}$) of ^{11}B with $1h_{9/2}$ (0.0 MeV), $2f_{7/2}$ (0.9 MeV), and $1i_{13/2}$ (1.63 MeV) of ^{209}Bi are well resolved and hence their yields are extracted separately. The differential elastic scattering cross sections, normalized to Rutherford cross sections, are plotted in Fig. 1. The data available in the literature [4] for $E_{\rm lab} = 118$ MeV, are also plotted. The statistical errors on the elastic scattering cross sections are typically $\simeq 1\%$ over the entire angular range at near and below barrier energies and for energies well above the barrier it is about 3% towards extreme backward angles. The errors remain within the size of the circle representing the data points except for a very few points at backward angles.

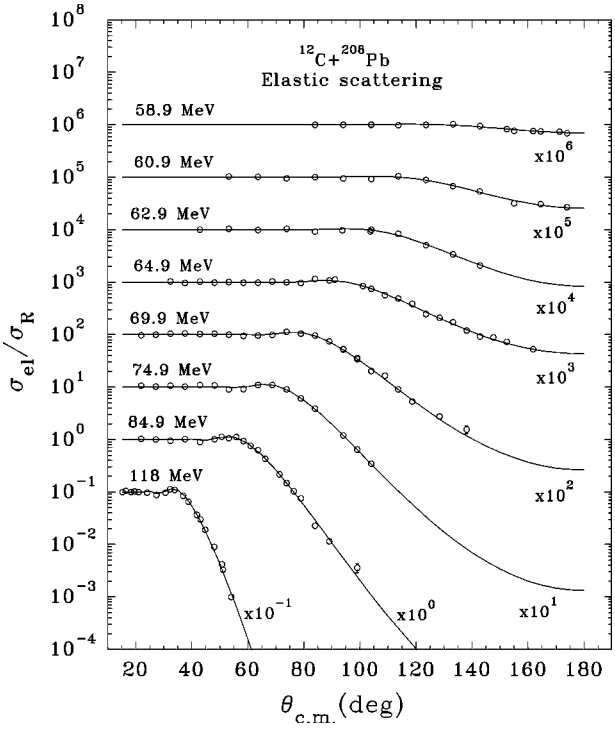

FIG. 1. Elastic scattering angular distributions for ^{12}C+^{208}Pb at different laboratory energies. The solid lines represent the optical model fits to the data.

III. OPTICAL MODEL ANALYSIS

A. Phenomenological analysis

A systematic optical model analysis of the elastic scattering differential cross sections for all the above energies was performed. The volume Woods-Saxon form for the real and the imaginary potential, was used. The total potential is defined as

$$U(r) = V_c(r,r_c) - \{V(r) + iW(r)\}, \tag{1}$$

where $V(r) = V_0 f_0(r)$ and $W(r) = W_0 f_w(r)$. Here V_0 and W_0 are the strengths of the real and the imaginary potentials, respectively, and the Woods-Saxon form factors are given by

$$f_x(r) = \frac{1}{1 + \exp\left(\dfrac{r - R_x}{a_x}\right)}, \tag{2}$$

where $R_x = r_x(A_P^{1/3} + A_T^{1/3})$ with $x = 0$ or w corresponding to real or imaginary parts of the potential, respectively. A_P and A_T are the projectile and the target masses, respectively. The Coulomb potential, $V_c(r,r_c)$ was taken as that due to a uniformly charged sphere of radius $R_c = r_c(A_P^{1/3} + A_T^{1/3})$ with r_c fixed at 1.2 fm. It has the form

$$V_c(r) = \begin{cases} \dfrac{Z_P Z_T e^2}{2R_c}[3 - (r/R_c)^2] & \text{for} \quad r < R_c \\ \dfrac{Z_P Z_T e^2}{r} & \text{for} \quad r > R_c\,. \end{cases} \tag{3}$$

Optical model parameter searches were carried out where all six parameters, i.e., strength, radius, and diffuseness of real and imaginary potentials are allowed to vary to achieve the best fit to the data. The parameters obtained from the fits to the experimental elastic scattering data at various energies are given in Table I.

The strong absorption radius, at any energy, was computed (Table I) from the formula for the distance of closest approach for the Coulomb trajectories, i.e.,

$$R_{sa} = \frac{\eta}{k}\left[1 + \left\{1 + \left(\frac{L_{1/2}}{\eta}\right)^2\right\}^{1/2}\right]. \tag{4}$$

TABLE I. Optical model (phenomenological) parameters from elastic scattering analysis. N is the number of data points for respective energies.

$E_{\rm lab}$ (MeV)	V_0 (MeV)	r_0 (fm)	a_0 (fm)	W_0 (MeV)	r_w (fm)	a_w (fm)	σ_{reac} (mb)	χ^2/N	R_{sa} (fm)
58.9	74.13	1.282	0.426	3.95	1.261	0.313	20	1.1	
60.9	55.64	1.282	0.483	56.49	1.261	0.384	136	6.5	12.50
62.9	52.57	1.282	0.481	51.58	1.261	0.432	286	4.5	12.54
64.9	65.50	1.282	0.463	163.71	1.265	0.365	429	6.2	12.55
69.9	51.74	1.282	0.444	25.73	1.268	0.502	715	4.4	12.39
74.9	86.94	1.282	0.395	18.81	1.256	0.527	969	7.8	12.34
84.9	31.07	1.282	0.473	25.66	1.256	0.527	1373	8.4	12.18
118.0	7.43	1.280	0.684	26.93	1.118	0.824	2218	5.7	11.87

Here, k is the wave number, η is the Sommerfeld parameter, and $L_{1/2}$ is the partial wave for which the transmission coefficient is 0.5, at the above energy. The mean value for R_{sa} was estimated to be 12.3 fm. Using the data from Table I, the values of the real and the imaginary potentials are calculated at $r=12.3$ fm and are plotted as a function of energy in Fig. 2. The errors on the potentials represent the difference between two extreme values of the potential where χ^2 becomes twice of the best fit value, and are obtained by varying V_0 and W_0 on either side of its best fit value in the optical model fit to the elastic scattering data.

B. Microscopic analysis

The elastic scattering data were also analyzed using a folding model potential [5]. The double folded potential for the system ^{12}C+^{208}Pb may be written as

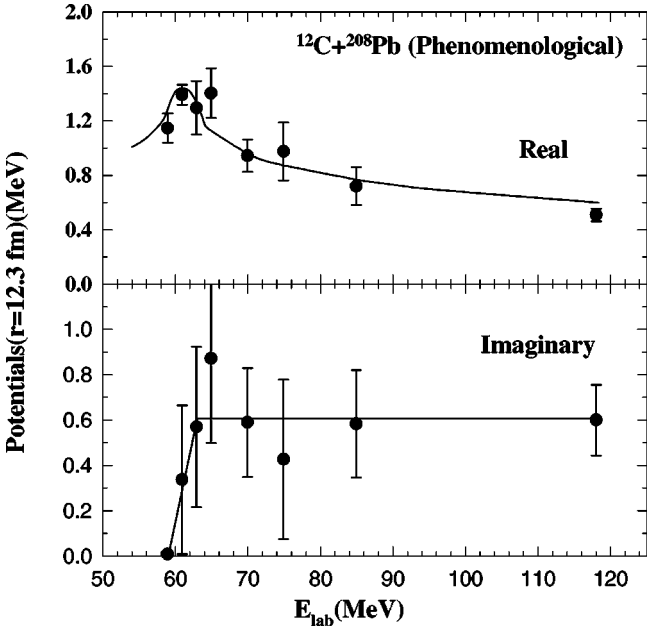

FIG. 2. Real and imaginary parts of the optical potentials at $r=12.3$ fm, obtained from the phenomenological analysis. The imaginary potential has been represented in the form of two straight line segments, and the resulting real potential calculated on the basis of the dispersion relation is shown as a continuous curve.

$$V_F=\int\int d\mathbf{r}_1 d\mathbf{r}_2 \rho(\mathbf{r}_1)\rho(\mathbf{r}_2)v(\mathbf{r}_{12}), \tag{5}$$

where $\mathbf{r}$ is the separation of the centers of mass of the two colliding nuclei, v is the effective nucleon-nucleon interaction, and the ρ's are point nucleon densities of ^{12}C and ^{208}Pb. The potentials were computed using the code DFPOT [6]. The interaction used was of the M3Y form [5], given by

$$v(r)=7999\frac{e^{-4r}}{4r}-2134\frac{e^{-2.5r}}{2.5r}+J_{00}\delta(r), \tag{6}$$

where the third term accounts for knockon exchange with $J_{00}=-265$ MeV fm^3. For the densities ρ_1 and ρ_2, the charge density distributions obtained by fiting the electron scattering data and parameterized in the Fermi parabolic form

$$\rho(r)=\frac{\rho_0(1+wr^2/c^2)}{1+\exp\left(\frac{r-c}{a}\right)}, \tag{7}$$

with $c=2.355$ fm, $a=0.522$ fm, and $w=-0.149$ for ^{12}C, and $c=6.624$ fm, $a=0.549$ fm, and $w=0$ for ^{208}Pb [7] were used. The ρ_0 values were chosen so as to normalize the distribution to their respective charge numbers. The point nucleon densities were obtained from the charge densities after correcting for the finite size of the proton in the standard way [5], using the root mean square values of the radii, $\langle r^2\rangle^{1/2}=2.455$ and 5.521 fm of ^{12}C and ^{208}Pb, respectively. The potential used to carry out the fits to the elastic scattering data was of the form

$$U(r)=-\lambda V_F(r)-iW(r)+V_c(r). \tag{8}$$

In the analysis, the folded real potential $V_F(r)$, was allowed an overall adjustable normalization coefficient λ. The forms of the imaginary potential $W(r)$ and the Coulomb potential $V_c(r)$ were the same as that used in the phenomenological analysis of the data. The best fits were obtained by varying the parameters λ and $W(r)$. The parameters corresponding to best fits are listed in Table II. It can be seen that there exists a strong energy dependence in the values of λ.

TABLE II. Optical model (microscopic) parameters from elastic scattering analysis.

E_{lab} (MeV)	λ	W_0 (MeV)	r_w (fm)	a_w (fm)	σ_{reac} (mb)	χ^2/N	R_{sa} (fm)
58.9	1.87	19.61	1.261	0.416	14.5	1.2	
60.9	2.32	46.81	1.257	0.399	130	6.8	12.50
62.9	2.18	52.46	1.261	0.430	282	5.0	12.52
64.9	2.36	148.45	1.264	0.362	415	5.2	12.50
69.9	1.83	47.64	1.262	0.441	695	4.2	12.38
74.9	1.67	34.95	1.256	0.492	965	9.5	12.33
84.9	1.25	25.56	1.256	0.536	1370	8.1	12.17
118.0	0.59	20.30	1.105	0.890	2186	8.2	11.85

Both the phenomenological and the microscopic analysis yielded real and imaginary potentials that are in good agreement with each other. The consistency between the real and the imaginary potentials can be easily tested by a dispersion relation [8]. The nucleus-nucleus optical potential can be expressed in a local and angular momentum independent form as

$$V(r,E)=V(r)+\Delta V(r,E)+iW(r,E), \tag{9}$$

where $\Delta V(r,E)$ is the dispersive term arising from the energy dependent imaginary part $W(r,E)$ through the dispersion relation,

$$\Delta V_{E_s}(r,E)=(E-E_s)\frac{P}{\pi}\int \frac{W(E')}{(E'-E_s)(E'-E)}dE', \tag{10}$$

where P is the principal value of the integral, E_s is a suitable reference energy, and

$$\Delta V_{E_s}(r,E)=V(r,E)-V(r,E_s). \tag{11}$$

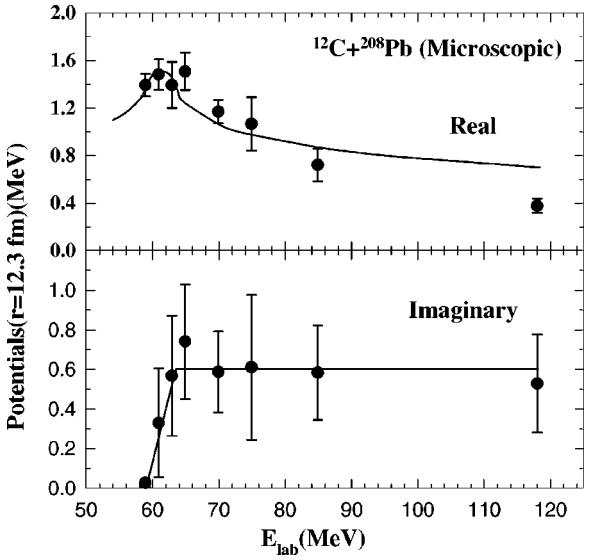

FIG. 3. Same as Fig. 2 but with microscopic analysis.

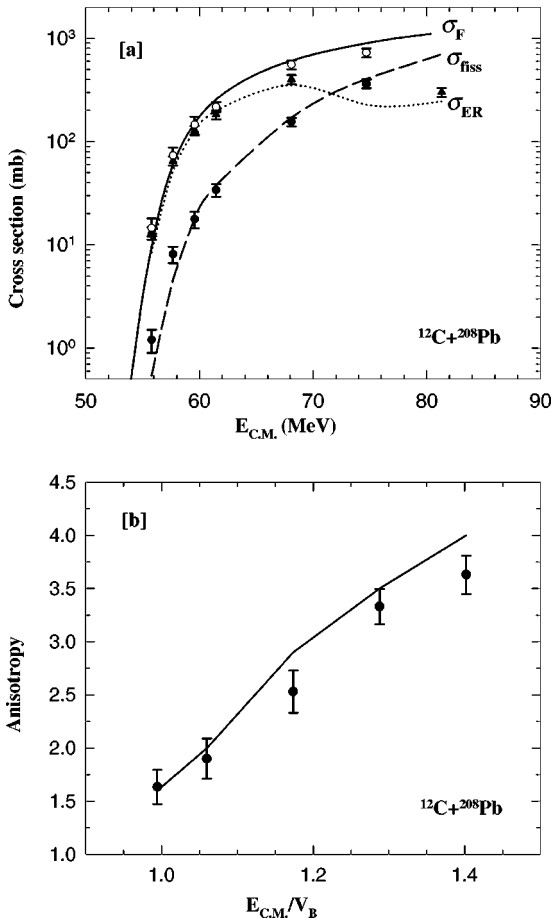

FIG. 4. Experimentally measured (a) fission (σ_{fiss}, filled circles), fusion (σ_F, open circles), and ER (σ_{ER}, filled triangles) cross sections, and (b) fission anisotropies at different energies. The solid line corresponding to the fusion was obtained from the CRC calculations. The long-dashed (fission), and the short-dashed (ER) lines, in (a), are obtained from the statistical model calculation. The continuous line (fission anisotropy) in (b) is the saddle-point model prediction.

This is known as the subtracted dispersion relation. The real and imaginary parts of the potentials calculated at the strong absorption radius $r=12.3$ fm, using the parameters obtained from the phenomenological and the microscopic analysis, are plotted as a function of bombarding energy in Figs. 2 and 3 respectively. The imaginary part of the potential is represented in the form of two straight line segments and the real part of the potential calculated using the dispersion relation is shown by the continuous curve. The referrence potential at $E_{lab}=118.1$ MeV was taken to be 0.65 MeV. It can be seen that the optical model (both phenomenological and folding model) analysis clearly establish the threshold anomaly for the present system.

IV. FUSION CROSS SECTIONS

The fission fragment angular distributions for ^{12}C $+^{208}$Pb system were measured at energies 58.9, 60.9, 62.9, 65, 72, and 79 MeV, in the angular range of 80°–170°. Two telescopes ($\Delta E-E$) of SSB detectors were used. One moni-

TABLE III. Evaporation residues for $2n$, $3n$, $4n$, and $5n$ channels.

E_{lab} MeV	σ_{2n} (mb)	σ_{3n} (mb)	σ_{4n} (mb)	σ_{5n} (mb)
58.9	10.4±2.1			
60.9	35.0±7.0			
62.9	27.0±5.4			
65		160	7.5	
72		195	205	
79		4.9	260	100
86			81	220
Reference	Present work	[9]	[9]	[9]

tor (single SSB detector) was kept at 40° for normalization. The evaporation residue (ER) cross sections for $3n$, $4n$, and $5n$ channels at energies 65, 72, 79, and 86 MeV were available in the literature [9]. The residue cross sections for the $2n$ channel have been measured in the present work by α counting at energies 58.9, 60.9, and 62.9 MeV to supplement the ER measurement. For ER measurements, three targets (with thin aluminum catcher foils on the back) were irradiated at different energies (58.9, 60.9, and 62.9 MeV) for 5 h each to populate the compound nucleus (CN) ^{220}Ra. After two-neutron evaporation and α decay of the daughter and grand daughter, the CN populates ^{210}Po, which has a half-life of 138 d. The α activity of ^{210}Po has been measured to determine the $2n$ ER cross sections. The activity of catcher foil was also taken into account.

The angle integrated fission cross sections, σ_{fiss}, obtained from the angular distribution data, are shown in Fig. 4(a) as filled circles. The measured ER data for $2n$ together with the existing data for $3n$, $4n$, and $5n$ (as read from [9]) are given in Table III. The total ER $(2n+3n+4n+5n)$ cross sections are shown as filled triangles in Fig. 4(a). Fusion cross sections, σ_F, are determined by adding σ_{fiss} with the corresponding ERs at all the above energies and are shown in Fig. 4(a) as open circles. A fit to the fusion data [solid line in Fig. 4(a)] was obtained by the CRC calculations using FRESCO [10] including all the significant channels as described in Sec. V. The potential used was of Woods-Saxon form with $V_0=50.0$ MeV, $r_0=1.2$ fm, and $a_0=0.63$ fm. Since, the aim of the present work was to achieve a simultaneous explanation of all the elastic and the nonelastic channels, the l distributions for each energy, generated from the FRESCO calculations, have been used as input to the statistical model (SM) code PACE2 [11] to compare with the fission and the ER data. In Fig. 4(a), long-dashed line corresponding to fission, and short-dashed line corresponding to total ER, were obtained from the SM fit to the data. Sierk values for the fission barrier (B_f), rotational energy (E_r), and effective moment of inertia (I_{eff}) were used in the calculation as starting values. The Sierk fission barrier was multiplied by a factor of 1.07 and the rotating liquid drop rotational energy was multiplied by a factor of 1.1, to obtain the best fit to the data. The values of the level density parameter a and the ratio of a_f to a_n were $A/9$ MeV^{-1} and 1.0, respectively,

TABLE IV. β's and deformation lengths for inelastic (vibrational) states used in the CRC calculations.

Nucleus	State	E_{level} of state (MeV)	β	Reduced deformation length (fm)
^{208}Pb	3^-	2.60	0.122	0.853
^{208}Pb	5^-	3.09	0.0802	0.575
^{208}Pb	2^+	4.18	0.05	0.418

where A is the atomic mass of the compound nucleus. Experimental mass was considered in the calculation of excitation energy.

Fission anisotropy has also been calculated to see how the system behaves at the energies around the Coulomb barrier. The anisotropies, $A=W(180°)/W(90°)$, were calculated using the saddle-point model by incorporating the presaddle neutron correction for each energy. As shown in Fig. 4(b), the calculated values of A (solid line) agree well with the experimental data (filled circles) implying that the present anisotropy data are ''normal.'' This observation is consistent with the earlier results obtained for other spherical target-projectile system [12].

V. CRC CALCULATIONS FOR ^{12}C+^{208}Pb

CRC calculations were performed with the code FRESCO, including all important channels that couple to the entrance channel, and the results are compared with the experimental data. Simultaneous description of elastic, inelastic, transfer, and fusion cross sections has been attempted by using the same set of potential parameters for all the energies. The full coupling scheme includes couplings to the 3^-, 5^-, and 2^+ states of ^{208}Pb and to a few states of the outgoing transfer partitions (^{13}C+^{207}Pb, ^{11}B+^{209}Bi, and ^{8}Be+^{212}Po). These are strongly populated, direct reaction channels. All the nonelastic channels are coupled to the entrance channel only.

The optical potentials in the elastic and the inelastic channels were assumed to be identical and consisted of the bare,

TABLE V. Particle-core binding energies and spectroscopic factors(C^2S values) for transfer states.

Nucleus	State (nlj)	E_x (MeV)	Binding energy (MeV)	C^2S	Ref.
^{13}C	$1p_{1/2}$	0.00	4.946	0.63	[16]
^{13}C	$2f_{5/2}$	3.089	1.857	0.95	[16,17]
^{207}Pb	$3p_{1/2}$	0.00	7.376	1.90	[18,19]
^{207}Pb	$2f_{5/2}$	0.570	7.947	5.60	[18,19]
^{207}Pb	$3p_{3/2}$	0.900	8.274	3.70	[18,19]
^{207}Pb	$1i_{13/2}$	1.630	9.006	12.2	[18,19]
^{11}B	$1p_{3/2}$	0.00	15.949	2.91	[16]
^{209}Bi	$1h_{9/2}$	0.00	3.791	0.95	[18,19]
^{209}Bi	$2f_{7/2}$	0.897	2.894	0.85	[18,19]
^{209}Bi	$1i_{13/2}$	1.613	2.178	0.70	[18,19]
^{8}Be	0^+	0.00	7.365	0.48	[20]
^{212}Po	0^+	0.00	1.000	1.69	[3]

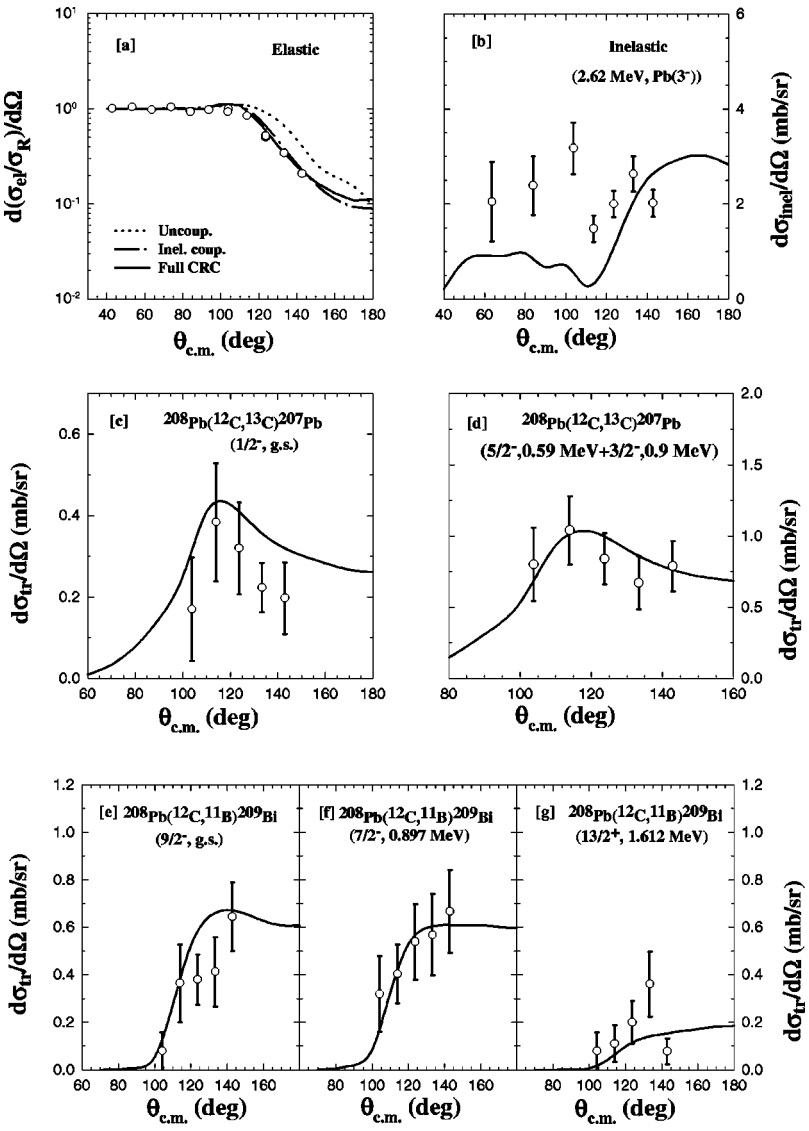

FIG. 5. The experimental and the CRC calculated angular distributions for (a) the ratio of elastic to Rutherford, (b) inelastic (3^-, 2.60 MeV, of ^{208}Pb), the ^{208}Pb(^{12}C,^{13}C)^{207}Pb reaction populating ^{13}C ground state with (c) $3p_{1/2}$, g.s., and (d) $2f_{5/2}$, 0.57 MeV+$3p_{3/2}$, 0.9 MeV states of ^{207}Pb, and ^{208}Pb(^{12}C,^{11}B)^{209}Bi reaction populating the ^{11}B ground state with (e) $1h_{9/2}$, g.s., (f) $2f_{7/2}$, 0.9 MeV, and (g) $1i_{13/2}$, 1.61 MeV states of ^{209}Bi, at $E_{\rm lab}=62.9$ MeV.

real potential of Woods-Saxon form with parameters $V_0=50.0$ MeV, $r_0=1.2$ fm, and $a_0=0.63$ fm and a Woods-Saxon squared imaginary potential of depth 50 MeV with a radius parameter of 1.0 fm and a diffuseness parameter of 0.4 fm. The interior imaginary potential provides an effective ingoing wave boundary condition for fusion and ensures that any surface absorption was due entirely to the couplings. Fusion is defined as the total absorption due to the interior imaginary potentials, those in the transfer partitions being of the same interior form as the entrance channel. Thus it is necessary to couple explicitly all nonelastic modes that occur at the nuclear surface. For transfer partitions, the real potentials were calculated using the semiempirical parametrization of folding model potentials given by Broglia and Winther [13],

$$U_n(r) = -31.67\frac{R(A_1)R(A_2)}{R(A_1)+R(A_2)} \times\left[1+\exp\left(\frac{r-R(A_1,A_2)}{a}\right)\right]^{-1} \quad \text{MeV}, \quad (12)$$

where $R(A)=1.233A^{1/3}-0.98A^{-1/3}$ fm and $R(A_1,A_2)=R(A_1)+R(A_2)+\Delta R$ fm with the diffuseness parameter set to $a=0.63$ fm and the free parameter $\Delta R=0.2$ fm. The real potential for the transfer partition, ^{11}B+^{209}Bi, when calculated in the surface region, using the above relation, are found to be in a very good agreement with that obtained from Ref. [14] at energy $E_{\rm lab}=84.1$ MeV (where the potential is expected to be free of coupling effects). The imaginary parts are exactly same as that of the entrance channel. The potentials binding the transferred particles were of Woods-Saxon form, with radius $1.2A^{1/3}$ fm and diffuseness 0.6 fm, their depths being automatically adjusted to obtain the required binding energies. The parameters of the real potential was first taken to be the same as that obtained from the phenomenological analysis at $E_{\rm lab}=84.9$ MeV as starting values.

The inelastic states were treated as collective (vibrational) states and their form factors were chosen to be the derivatives of the potentials. The β values [15] and the deformation lengths are listed in Table IV. The particle-core binding energies and their spectroscopic factors (C^2S values

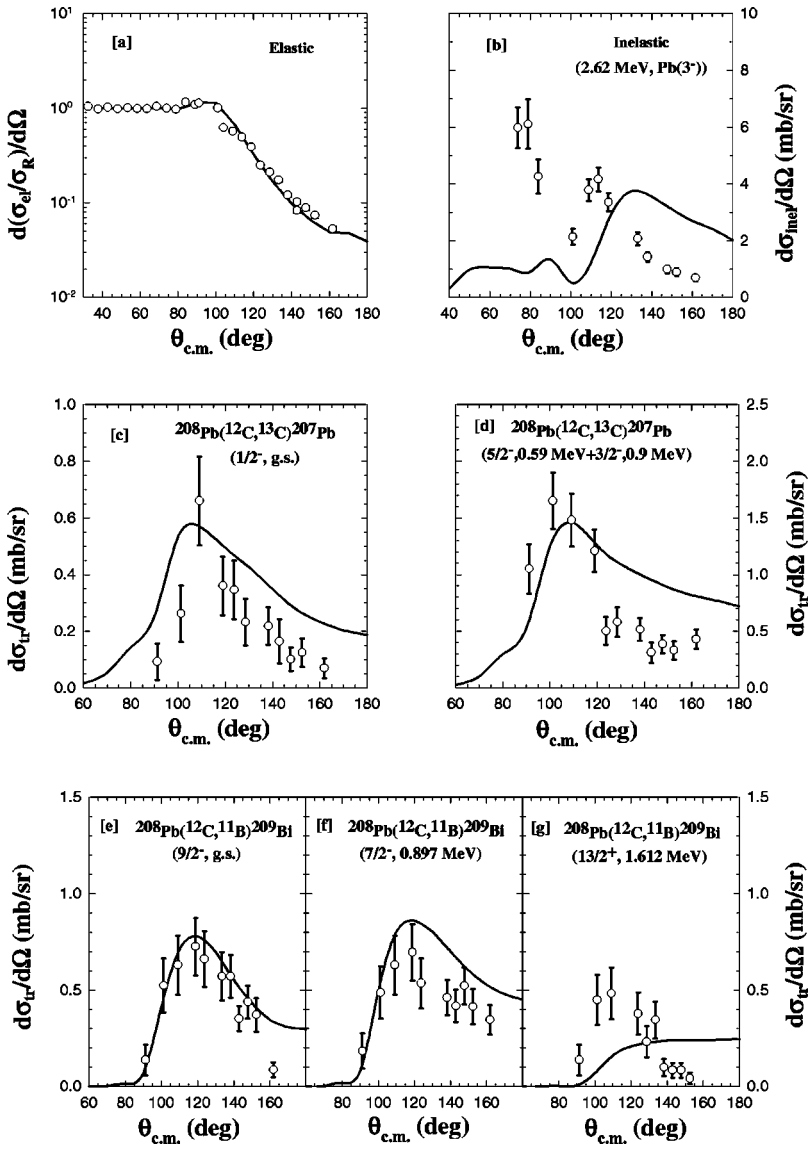

FIG. 6. Same as in Fig. 5 but for $E_{\mathrm{lab}} = 64.9$ MeV.

[16–20]), which are used in the CRC calculations for nucleon transfer channels are listed in the Table V. The strength of the α transfer was taken to be the same as that in the case of ^{209}Bi(^{12}C,^{8}Be)^{213}At in Ref. [3].

The full CRC calculations including as many as 20 significant channels were performed using the above information in the energy range of 50–86 MeV, in steps of 1 MeV. The same set of channels and coupling parameters were used throughout and no energy dependent parameter was introduced in the analysis. It may be noted that the attempt here is rather to use the structure information available in the literature and predict the cross sections instead of trying to fit the experimental data by varying the parameters. The CRC results for elastic and some of the inelastic and the transfer angular distributions were compared with the experimental data at three energies, two near barrier (62.9 and 64.9 MeV), and one well above the barrier (84.9 MeV), in Figs. 5, 6, and 7, respectively. The effect of couplings of inelastic and transfer channels on the elastic scattering at 62.9 MeV is shown in Fig. 5(a). The dotted, dashed, and solid lines correspond to the CRC calculations without any coupling, with inelastic coupling, and with full (inelastic + transfer) coupling respectively. Figures 5(b), 6(b), and 7(b) show the inelastic angular distributions corresponding to Pb (3^-, 2.62 MeV) state. The angular distributions corresponding to the ^{208}Pb(^{12}C,^{13}C)^{207}Pb reaction populating the ^{13}C ground state with (i) $3p_{1/2}$, 0 MeV, and (ii) $2f_{5/2}$, 0.57 MeV $+3p_{3/2}$, 0.9 MeV states of ^{207}Pb are plotted in Figs. 5(c), (d), 6(c),(d), and 7(c),(d). The angular distributions corresponding to the ^{208}Pb(^{12}C,^{11}B)^{209}Bi reaction populating the ^{11}B ground state with (i) the $1h_{9/2}$, 0 MeV, (ii) $2f_{7/2}$, 0.9 MeV, and (iii) $1i_{13/2}$, 1.61 MeV states of ^{209}Bi are plotted in Figs. 5(e)–(g), 6(e)–(g), and 7(e)–(g). Although, there were several channels included in the full CRC calculations, the results are compared with the experimental data for only seven channels that have been analyzed. It can be seen from Figs. 5, 6, and 7 that there is a good agreement between the results of the CRC calculations and the experimental data corresponding to the elastic and the nonelastic channels for all three energies. The experimental values of the inelastic cross sections in the forward angles are larger than the calculated ones. This may be due to inclusion of the elastic tail

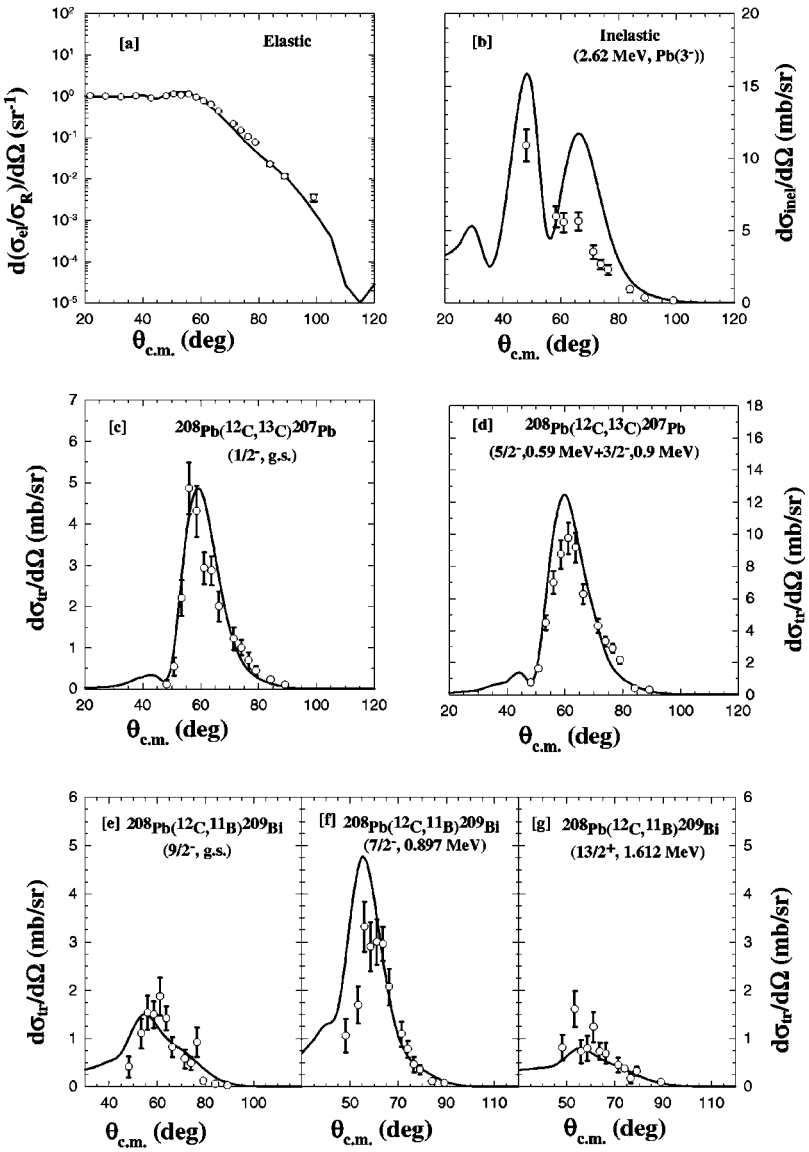

FIG. 7. Same as in Fig. 5 but for $E_{\rm lab} = 84.9$ MeV.

under the inelastic peak in the analysis of data. The combined values of elastic and inelastic cross sections have been compared with the calculations (not shown in the figure) and they match very well in the whole angular range. As pointed out earlier, the calculated fusion excitation functions, plotted in Fig. 4(a), also agree with the experimental data. The simultaneous description of elastic, inelastic, transfer, and fusion data over the wide range of energy and angular distribution ensures that the real potential used for the entrance channel in the CRC calculations, can be considered as the bare nucleus-nucleus potential. The effective potential [21] that was obtained by adding the polarization potential to the bare potential evaluated at $r = 12.3$ fm is compared in Fig. 8 with the energy dependent potentials obtained from the microscopic optical model analysis. The solid line represents the effective (bare plus polarization) potential obtained by the CRC calculations with full couplings. The depth of the effective potential increases at and around the barrier showing the correct trend similar to that of the optical potential determined from the elastic scattering analysis. It may be relevant to point out that the bare potential can also be obtained by another approach that is employed by Silva *et al.* [22] for ^{16}O+^{208}Pb system.

VI. QUASIELASTIC BARRIER DISTRIBUTION

The effects of couplings of various inelastic and transfer channels on the elastic and the fusion channels at near barrier energies can also be observed in the fusion BD in the form of multiple peaks or a shoulder depending upon the strength and excitation energy of each coupling [23]. One way to obtain the representation of fusion barrier distributions is from QE scattering as suggested by Timmers *et al.* [24]. Since, for the present system (^{12}C+^{208}Pb), (i) there are no significant transfer channels with positive Q values, and (ii) the target is spherical, one can expect that vibrational excitation will dominate over rotation and nucleon exchange, and thus barriers higher than the uncoupled barrier will give more information regarding the coupling effects. Thus it is desirable to have accurate BD data in the region of higher barriers that can be obtained better by the QE method be-

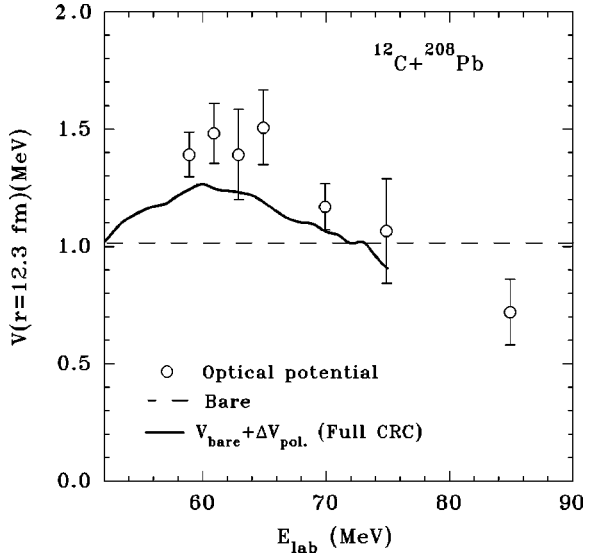

FIG. 8. Effective (bare + polarization) potential vs $E_{\rm lab}$. The hollow circles represent the real part of the optical potential obtained from microscopic analysis and calculated at $r=12.3$ fm. The solid line is obtained by adding the polarization potential obtained from the CRC calculations to the bare potential (dashed line) considered for the elastic and inelastic partition.

cause the errors on the BD calculated from fusion excitation functions in this region are very large. It has also been shown [25] that one has to be careful about the effect of long range absorption on higher fusion barriers while estimating fusion by an optical model. Here, the couplings lead to change in the shape of the BD for the higher barriers, which cannot be distinguished within the large experimental errors of the BD obtained from the fusion excitation function. However, the small error on the QE data at this region of the barriers makes it more sensitive to a small deviation due to the above effects. As concluded in Ref. [26], the dynamics of the fusion of two colliding nuclei and their structure information cannot be obtained unambiguously just from the fusion BD study. One needs to study all the aspects of the reaction (i.e., fusion and quasielastic) simultaneously that should be explained by the same set of potentials and coupling parameters in CRC calculations at all the energies. Thus, the quasielastic BD will be an important constraint to choose the bare potential while performing the CRC calculations consistently.

The QE excitation functions have been measured using two telescopes at $\pm 170°$ in the energy range of 51–73 MeV in steps of 1 MeV. Two monitors were kept at $\pm 30°$ for normalization. The ^{208}Pb target used was of thickness $\approx 160\ \mu$g/cm^2 sandwiched between thin films of carbon ($\approx 40\ \mu$g/cm^2) and nickel ($\approx 40\ \mu$g/cm^2).

The measured differential cross sections relative to the Rutherford scattering cross sections for elastic, elastic +inelastic (3^- of Pb), elastic+inelastic (3^- and 2^+ of ^{208}Pb and 2^+ of ^{12}C), and quasielastic (elastic+inelastic +transfer) cross sections have been shown in Fig. 9(a). The corresponding values of the first derivatives of the quantity ''$-\sigma_{QE}/\sigma_{Ruth}$''with respect to energy E as in Ref. [24], are derived and are shown in Fig. 9(b). The distribution shows a

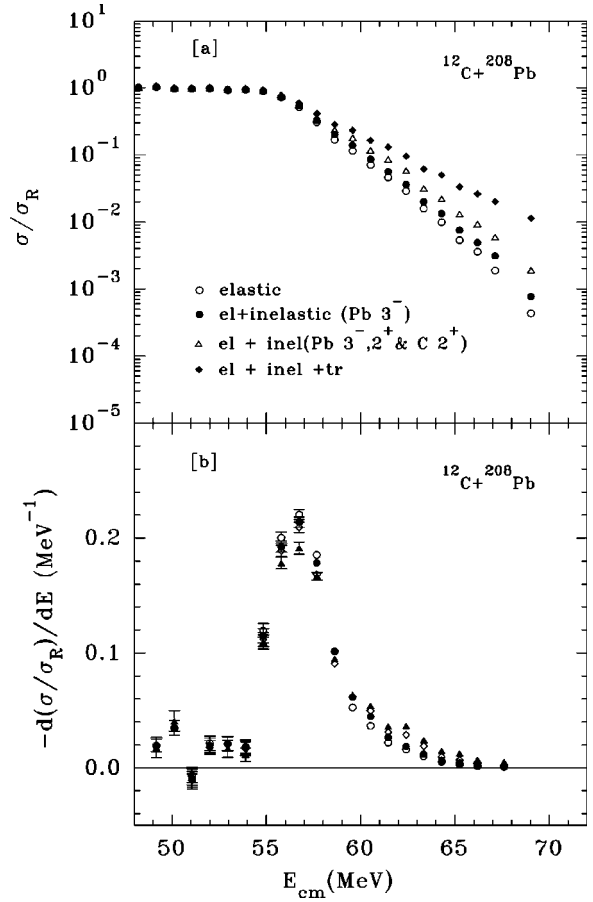

FIG. 9. (a) Ratio of the measured differential cross sections to the Rutherford scattering for elastic, elastic + inelastic (3^- of ^{208}Pb), elastic + inelastic (3^- and 2^+ of ^{208}Pb and 2^+ of ^{12}C), and quasielastic (elastic + inelastic + transfer) channels, and (b) their corresponding first derivatives of the quantity ''$-\sigma_{QE}/\sigma_{Ruth}$'' with respect to E.

long tail in the region of higher barriers instead of distinct peaks corresponding to different couplings as seen in the fusion barrier distributions for some cases [23]. With the increasing number of channels added to the elastic scattering, the tail becomes more prominent. From the excitation functions measured for each channel [Figs. 10(a) and 10(b)], the components of the BD are derived in order to know their individual contributions to such structure and are shown in Figs. 10(c) and 10(d). It can be seen from Fig. 10(c) that, the shoulder structure is mainly due to the inelastic components of the BD. The components of the BD corresponding to the Q-integrated transfer channels [Fig. 10(d)] have negligible contributions in this region of the barriers.

The QE excitation functions obtained from the CRC calculations (using the parameters same as discussed in Sec. V) and the BDs derived from it are compared with the experimental data in Figs. 11(a) and 11(b), respectively. The dash-dot-dot and the continuous lines in Fig. 11(b) correspond to elastic+inelastic and elastic+inelastic+transfer, respectively, and they are in good agreement with the data.

In the results of the CRC calculations, shown in these figures, the coupling to the quadrupole excitation of the pro-

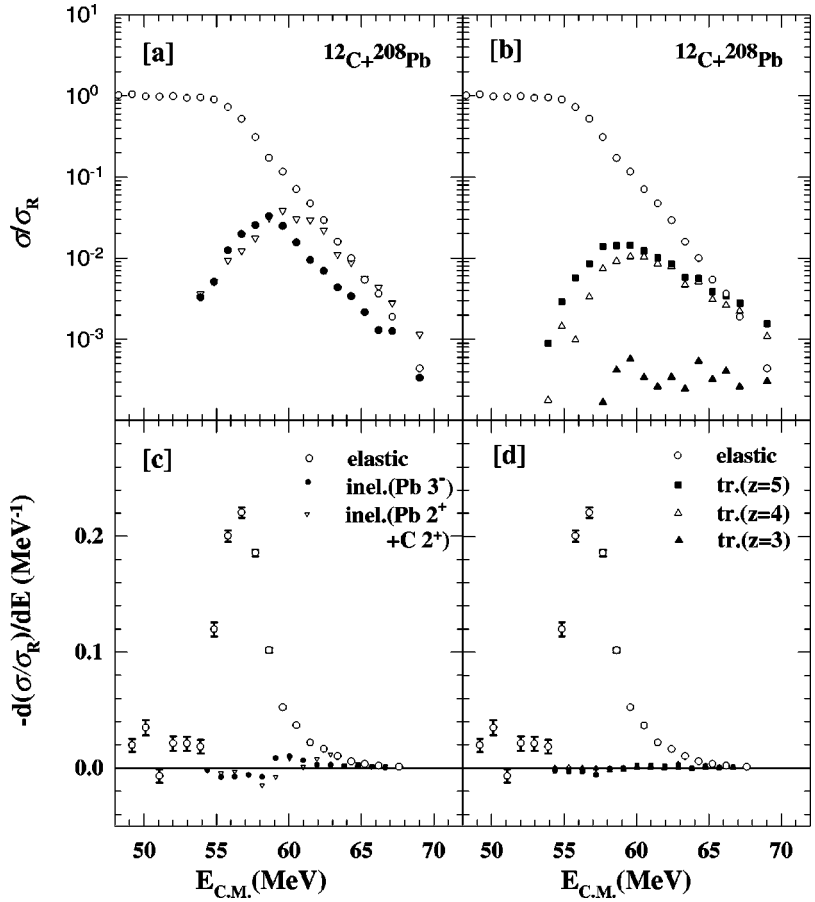

FIG. 10. Individual differential cross sections normalized to the Rutherford scattering for (a) elastic, inelastic (3^- of ^{208}Pb only), inelastic (2^+ of ^{208}Pb+2^+ of ^{12}C), (b) elastic, ^{11}B ($Z=5$), ^{10}Be+^{9}Be ($Z=4$), and ^{7}Li+^{6}Li ($Z=3$), and their corresponding components of the barrier distribution in (c) and (d), respectively.

jectile was not considered. Inclusion of the quadrupole excitation of the projectile deteriorates the matching of the CRC results of both the quasielastic excitation function, and the resultant barrier distribution (particularly in high-energy region) with the experimental data. It has been pointed out [23,27] that, the use of linear coupling approximation (LA) for states of $E_x \geqslant \hbar\omega$ (barrier curvature energy), in the BD analysis, is not justified. Interestingly, the CRC calculations with LA for 2^+ of projectile seems to work well in reproducing σ_F and angular distributions (limited to small θ range) of other dominant channels at high energy. This might imply that the use of LA in the CRC calculations with projectile excitation ($E_x=4.4$ MeV) has more influence on the QE data measured at high energy and for large θ ($\approx 170°$) values. It may also be pointed out that a calculation of QE (elastic + inelastic only) using ECIS [28] yields results that agree with the CRC values over the entire energy range. However, the pronounced oscillation in QE cross sections at high energy predicted by CRC is not reproduced by ECIS calculation.

To see the effect of individual channel on the excitation functions of elastic and fusion, and the BD obtained from fusion, the CRC calculations were performed by coupling different channels. The calculated values were compared with the experimental data (BD was from QE data) in Figs. 12(a)–(c), respectively. The fusion barrier distributions were obtained from the second derivative of the quantity ''$\sigma_F E$'' with respect to energy E, normalized by a factor $1/\pi r_B^2$. The value of r_B was 11.45 fm. The CRC calculations with full coupling that included three inelastic states of ^{208}Pb, one-neutron pickup, one-proton stripping, and one-alpha stripping channels, provide very good agreement of the excitation functions and the BDs. This implies that the channels considered in the CRC calculations are sufficient for understanding the coupling mechanism involved in the present system. The couplings of only 3^- of Pb (dash-dot line) and 3^-, 2^+, and 5^- of Pb (dash-dot-dot line) have considerable effect on elastic, fusion, and BD obtained from fusion, as compared to the uncoupled results (Fig. 12). In both of these cases, the fusion cross sections were enhanced, the height of the main barrier was reduced, and the signature of a higher barrier became prominent. It was interesting to see that, the inclusion of transfer channels has also enhanced the fusion cross section, and improved the match between the BD obtained from the calculated fusion excitation functions and that from the experimental QE data. However, there is no significant effect of transfer coupling on the elastic excitation function [Fig. 12(a)].

To investigate the long range effect on higher fusion barriers [25], the CRC calculations are performed with different radius parameter of the short range imaginary potential, i.e., $r_w=1.0$ fm, 1.1 fm, and 1.15 fm. The excitation functions of elastic and fusion, and the BD obtained from fusion for the above three cases are shown in Figs. 13(a), (b), and (c), respectively. It can be observed that when the value of r_w is changed from 1.0 fm to 1.1 fm, the results do not change appreciably. However, the CRC results with a value $r_w=1.15$ fm deviates from the experimental data significantly

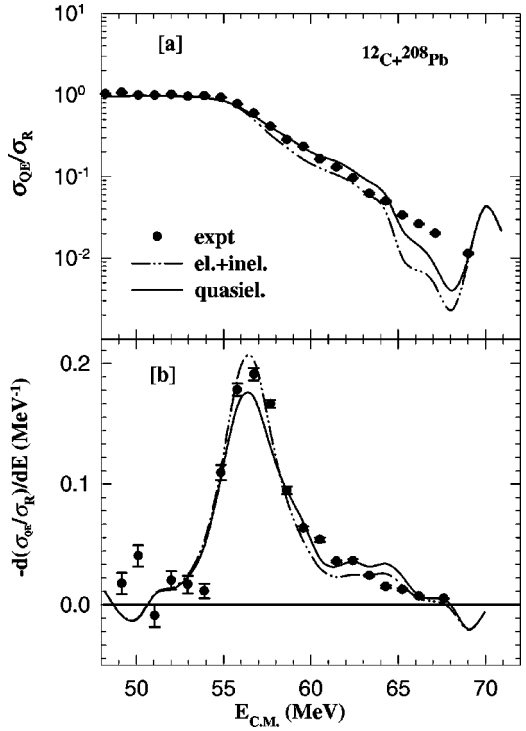

FIG. 11. (a) Quasielastic excitation functions at $\theta_{lab}=170°$, calculated from the CRC calculations, are compared with the experimental data (filled circles). The dash-dot-dot and the continuous lines correspond to elastic+inelastic and elastic+inelastic+transfer channels considered in the CRC calculations, and (b) their corresponding barrier distributions obtained by quasielastic method.

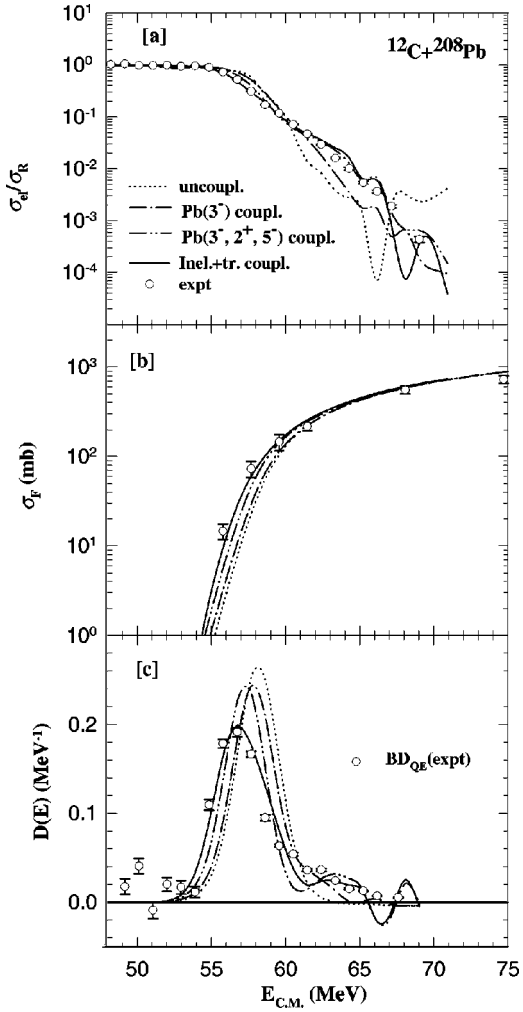

FIG. 12. Excitation functions of (a) elastic ($\theta_{lab}=170°$), and (b) fusion as obtained from CRC calculations using FRESCO, with different coupling, are compared with the uncoupled results (dotted line), and the experimental data (open circles). (c) The corresponding barrier distributions, obtained from the second derivative of the product ''$\sigma_F E$'' with respect to E (see text) are compared with the fusion barrier distribution obtained from quasielastic data.

in the region of higher barriers for both in elastic and fusion BD, although the fusion excitation functions for all three cases are almost the same. Therefore, one should limit on r_w to a maximum value of 1.1 fm, without interfering the region of direct reactions that might have been modified due to coupling. As suggested in Ref. [25], it is clear that BD from QE can be a tool to see the sensitivity of fusion on r_w.

COMPARISON BETWEEN $^{12}C+^{208}Pb$ AND $^{12}C+^{209}Bi$

The single particle configuration ($1h_{9/2}$) with nonzero ground state spin ($\frac{9}{2}\hbar$) of ^{209}Bi has only one extra odd proton compared to the doubly shell closed magic nucleus of ^{208}Pb. In ^{209}Bi, it has been observed [29] that the most dominant inelastic excitations are due to the particle-core vibrations. The group of seven states with $E_x \approx 2.492-2.751$ MeV appears to be well described as a multiplet formed by coupling a $1h_{9/2}$ single-particle proton state (^{209}Bi ground state) with the 3^- collective excitation at 2.614 MeV in ^{208}Pb. The energy of the septuplet centroid (2.62 MeV) and the combined value of β_3^2 (0.11) are similar to those for ^{208}Pb. A decuplet of states in ^{209}Bi with the centroid at 3.09 MeV corresponding to the 5^- of ^{208}Pb has similar value of β_5^2. The same is true for 4^+ and 2^+ states of ^{208}Pb. Therefore, no major difference in the coupling of the inelastic states (due to core excitations) on the entrance channel is expected. However, there are six single particle states (as predicted by shell model) in ^{209}Bi, which are not present in the case of ^{208}Pb. But the β values for these states are very small, and hence, due to their weak coupling to the entrance channel, no drastic effect on the effective nucleus-nucleus potential (obtained from optical model analysis of elastic scattering data), is expected. Some differences can be expected in the transfer channels as the Q values and spectroscopic factors are different for some of the transfer channels. For example, in the $1p$ pickup reactions ^{209}Bi,^{208}Pb(^{12}C,^{13}N), the Q values are -1.855 MeV and -6.068 MeV, respectively, implying the former case to be more favorable.

The optical potentials for the two systems are compared in Figs. 14 and 15 for different energies normalized to the Coulomb barrier. No significant difference was observed in the real part of the phenomenological potentials (Fig. 14) of the two systems. The potential values around the Coulomb barrier lie within the error bars. In the microscopic model the real potentials for the Bi case are somewhat smaller (Fig. 15)

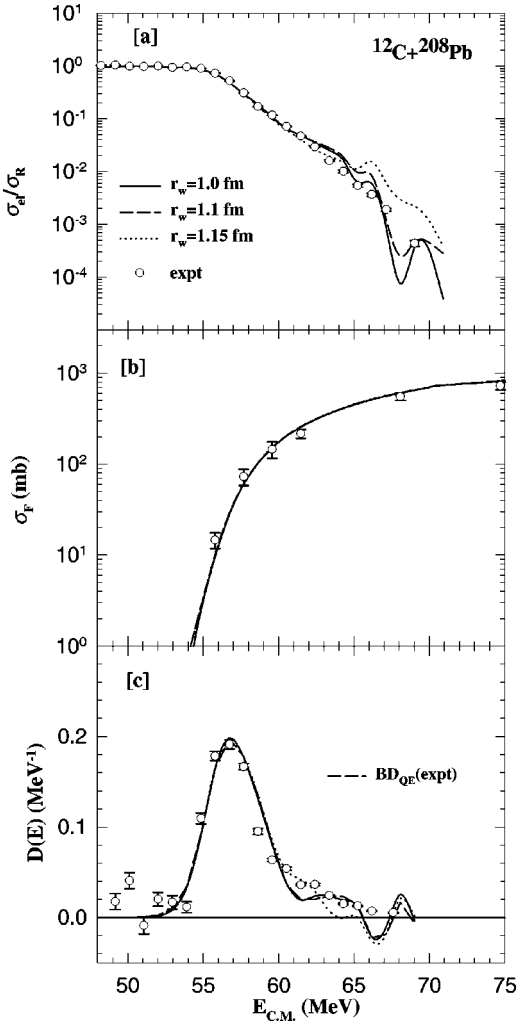

FIG. 13. Excitation functions of (a) elastic ($\theta_{\rm lab}=170°$), (b) fusion, and (c) BD obtained from fusion for $r_w=1.0$ fm (solid line), 1.1 fm (long-dashed line), and 1.15 fm (short-dashed line).

around the barrier region. This is due to different shapes used in the double-folded potential calculations. It is known that the potential is sensitive only in a small region around R_{sa}, the strong absorption radius. The value of R_{sa} for Bi case was 12.9 fm [3], where both phenomenological and microscopic potentials were the same. In the case of Pb too, the potentials obtained in the two models at the strong absorption radius R_{sa} ($=12.3$ fm) are similar.

The fission and the fusion excitation functions for both the systems are plotted in Fig. 16 at energies normalized to Coulomb barrier. Fission for Bi case is significantly higher than Pb case [Fig. 16(a)]. This can be understood in terms of fissility (Z^2/A) consideration. Also, for the same beam energies (normalized to Coulomb barrier), the compound nucleus excitation energies for the Bi case are larger (by 3.49 MeV) that will enhance the fission cross sections and hence consistent with the observation. The fusion cross sections obtained by the quasielastic method and measured by the authors for both the systems are compared in Fig. 16(b). The reaction cross sections obtained from the optical model analysis are also plotted in Fig. 16(c). The fusion and the reaction cross sections are similar for the two systems.

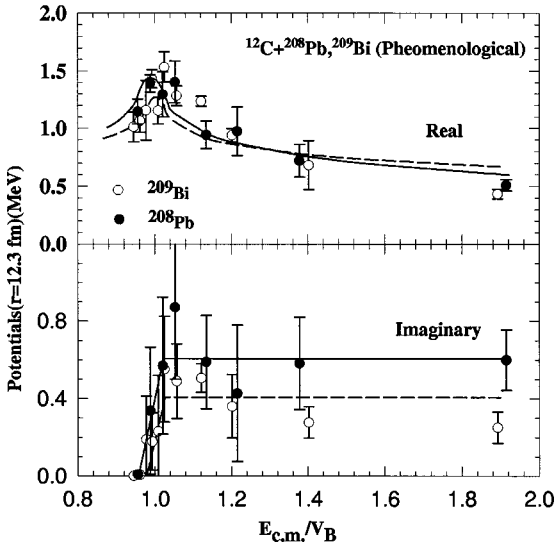

FIG. 14. Real part of the phenomenological potentials calculated at the radius $r=12.3$ fm for $^{12}C+^{208}Pb$ and $^{12}C+^{209}Bi$ system. The energies are normalized to the Coulomb barriers ($V_B=58.28$ and 58.97 MeV for Pb and Bi, respectively, in the center-of-mass system).

With the motivation to see the differences in some of the other reaction channels, the data of various transfer channels for the two systems was analyzed. At the near barrier energy ($E_{\rm c.m.}/V_{\rm B}\approx1.02$), the elastic, inelastic (3^- of ^{208}Pb core), and Q-integrated angular distributions for the reactions ^{208}Pb,^{209}Bi(^{12}C,^{13}C) and ^{208}Pb,^{209}Bi(^{12}C,^{11}B) are shown in Fig. 17(a)–(d), respectively.

The Q-integrated transfer angular distributions for (a) ^{13}C, (b) ^{11}B, (c) ^{10}Be, (d) ^{9}Be, (e) ^{7}Li+^{6}Li, and (f) inelastic (3^- of ^{208}Pb core) channels measured for ^{208}Pb,^{209}Bi(^{12}C,x) reactions at $E_{\rm c.m.}/V_{\rm B}\approx1.4$ are also extracted and compared in Fig. 18.

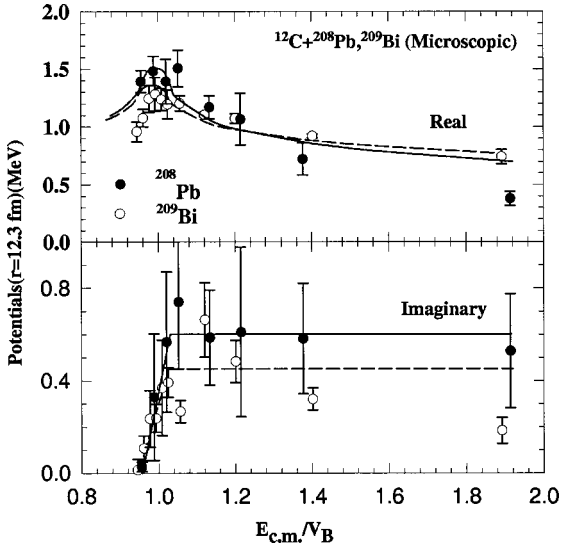

FIG. 15. Same as Fig. 13 but for microscopic analysis.

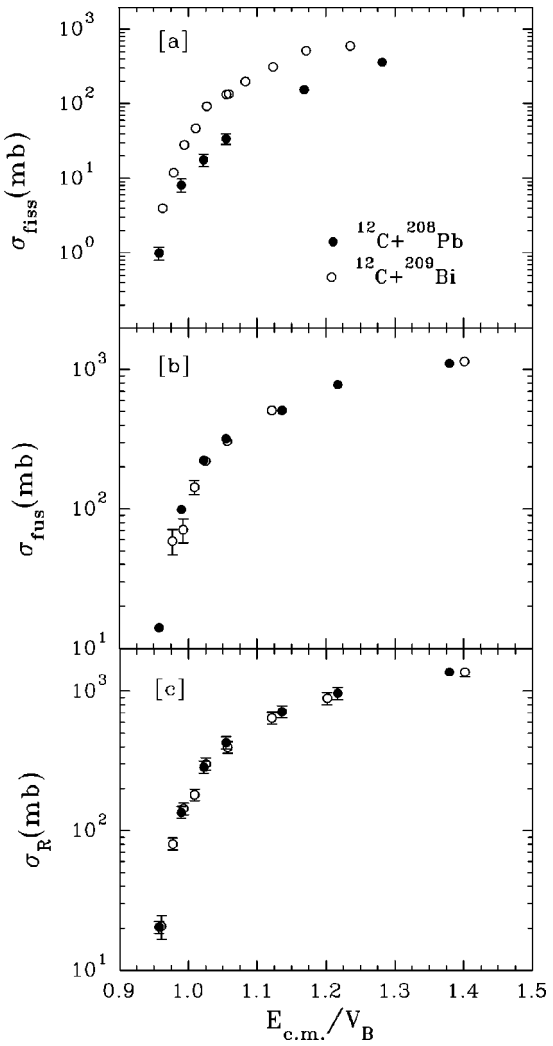

FIG. 16. (a) Fission, (b) fusion, and (c) reaction excitation functions for $^{12}C+^{208}Pb$ and $^{12}C+^{209}Bi$ systems.

No significant difference beyond the error bars on the respective data in the above channels was found between the two systems at approximately same energies normalized to barrier. Experimentally, the $1p$ pickup channel for both the systems, i.e., $^{209}Bi,^{208}Pb(^{12}C,^{13}N)$ was found to be negligible as the cross section was too low and was consistent with the CRC calculation. The effect on the elastic channel, due to the coupling of this transfer channel, is also calculated to be negligible, and hence, explain the similarity in the real part of the optical potential between the two systems.

VII. CONCLUSIONS

Elastic, inelastic, transfer, fission, and evaporation residue measurements for $^{12}C+^{208}Pb$ system, in the energy range of 58.9–84.9 MeV, are reported. Optical model (both phenomenological and microscopic) analysis of the data shows a large energy dependence of the optical potential particularly at near barrier energies as expected. The real part of the optical potential calculated by the dispersion relation, with

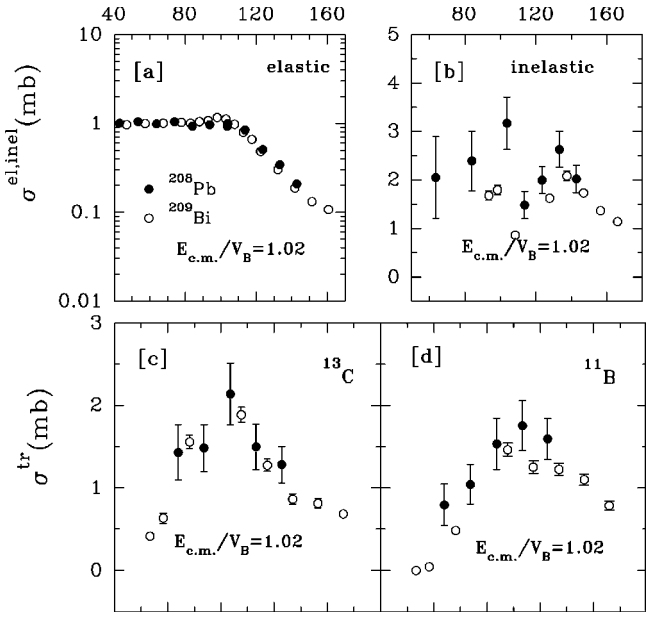

FIG. 17. Angular distributions for (a) elastic, (b) inelastic (3^- of ^{208}Pb core), (c) 1 n pickup (^{13}C, Q integrated), and (d) 1 p stripping (^{11}B, Q integrated) reactions at $E_{c.m.}/V_B \approx 1.02$.

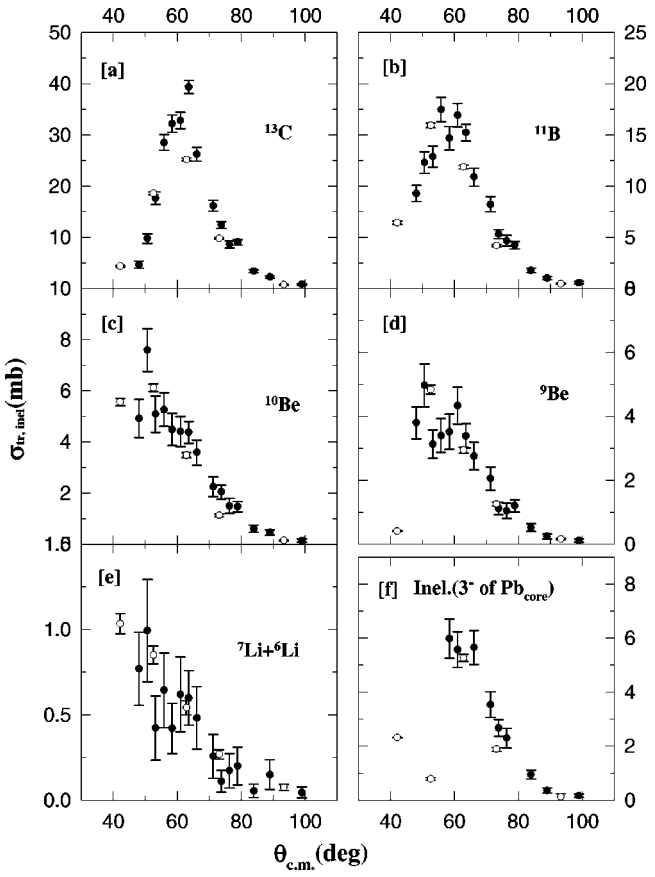

FIG. 18. Q-integrated transfer angular distributions for (a) ^{13}C, (b) ^{11}B, (c) ^{10}Be, (d) ^{9}Be, (e) ^{7}Li+^{6}Li, and (f) inelastic (3^- of ^{208}Pb core) channels measured for $^{208}Pb,^{209}Bi(^{12}C,x)$ reactions at $E_{c.m.}/V_B \approx 1.4$.

an assumed shape of the imaginary part and a reference real potential V_{ref}, reproduces the experimental values. A statistical model fit to both fission and fusion data at each energy has been achieved using the l distributions obtained from the CRC calculations. The measured fusion excitation function shows an enhancement at subbarrier energies as compared to those obtained without coupling in the CRC calculations. The results of the CRC calculations, which included a large number of inelastic and transfer channels, explained all the channels simultaneously at all the energies. The effective real potentials obtained from the CRC calculations are consistent with the observed energy dependence of the real part of the optical potential. A good agreement between the fusion barrier distributions obtained from quasielastic data and that obtained from both quasielastic and fusion excitation functions by the CRC calculations, was achieved. Thus the bare potential (of Woods-Saxon form with $V_0=50$ MeV, $r_0=1.2$ fm, and $a_0=0.63$ fm) used in the CRC calculations, with such a large number of constraints, can be considered as the unique nucleus-nucleus potential for $^{12}C+^{208}Pb$ system.

The effect of long range absorption was observed on elastic and BD obtained from fusion when the value of r_w was changed from 1.0 fm to 1.15 fm. An upper limit on radius parameter $r_w=1.1$ fm ensures the imaginary potential to be short ranged while calculating fusion for the present system by optical model. Thus, the BD obtained from QE data was found to an important tool to probe the sensitivity of fusion on r_w.

A comparison with the data for some of the dominant channels showed that, on the $E_{\mathrm{c.m.}}/V_{\mathrm{B}}$ scale, the two systems ($^{12}C+^{209}Bi$ and $^{12}C+^{208}Pb$) behave in a similar way. This indicates that the extra proton in ^{209}Bi does not have a significant effect on these channels as well as on the energy dependence.

ACKNOWLEDGMENTS

The authors thank U. K. Pal, V. Jha, A. Navin, and B. J. Roy for their help during one of the experiments of this program. Thanks are also due to the Pelletron crew, for the smooth operation of the accelerator during the experiments carried out for this work.

[1] L. C. Vaz and J. M. Alexander, Phys. Rev. C **10**, 464 (1974).
[2] C. Mahaux, H. Ngo, and G. R. Satchler, Nucl. Phys. **A449**, 354 (1986).
[3] S. Santra, P. Singh, S. Kailas, A. Chatterjee, A. Navin, A. Shrivastava, A. M. Samant, and K. Mahata, Phys. Rev. C **60**, 034611 (1999).
[4] A. M. Friedman and R. H. Siemssen, Phys. Rev. C **6**, 2219 (1972).
[5] G. R. Satchler and W. G. Love, Phys. Rep. **55**, 183 (1979).
[6] J. Cook, Comput. Phys. Commun. **25**, 125 (1982).
[7] C. W. De Jager, H. De Vries, and C. De Vries, At. Data Nucl. Data Tables **14**, 479 (1974).
[8] G. R. Satchler, Phys. Rep. **199**, 147 (1991).
[9] T. Nomura, K. Hiruta, T. Inamura, and M. Odera, Nucl. Phys. **A217**, 253 (1973).
[10] I. J. Thompson, Comput. Phys. Rep. **7**, 167 (1988).
[11] A. Gavron, Phys. Rev. C **21**, 230 (1980).
[12] G. V. Raviprasad, A. M. Samant, A. Shrivastava, A. Navin, A. Chatterjee, P. Singh, S. Kailas, and V. S. Ramamurthy, Phys. Rev. C **57**, 971 (1998); A. Samant, S. Kailas, A. Chatterjee, A. Shrivastava, A. Navin, and P. Singh, Eur. Phys. J. A **7**, 59 (2000).
[13] R. A. Broglia and A. Winther, *Heavy Ion Reactions*, Lecture Notes Vol. 1 (Benjamin, New York, 1981).
[14] A. Shrivastava, S. Kailas, P. Singh, A. Chatterjee, A. Navin, A. M. Samant, V. Ramdev Raj, S. Mandal, S. K. Datta, and D. K. Awasthi, Nucl. Phys. **A635**, 411 (1998).
[15] T. P. Cleary, Nelson Stein, and P. R. Maurenzig, Nucl. Phys. **A232**, 287 (1974).
[16] S. Cohen and D. Kurath, Nucl. Phys. **A101**, 271 (1967).
[17] L. Jarczyk, B. Kamys, Z. Rudy, A. Strazalkowski, and H. Witała, Phys. Rev. C **28**, 700 (1983).
[18] P. Ring and E. Werner, Nucl. Phys. **A211**, 198 (1973).
[19] K. S. Toth, J. L. C. Ford, Jr., G. R. Satchler, E. E. Gross, D. C. Hensely, S. T. Thornton, and T. C. Scheizler, Phys. Rev. C **14**, 1471 (1976).
[20] K. Umeda, T. Yamaha, T. Suchiro, K. Takimoto, R. Wada, E. Takada, S. Shimoura, A. Sakaguchi, S. Murakami, M. Fukada, and Y. Okuma, Nucl. Phys. **A429**, 88 (1984).
[21] I. J. Thompson, M. A. Nagarajan, J. S. Lilley, and M. J. Smithson, Nucl. Phys. **A505**, 84 (1989).
[22] C. P. Silva, M. A. G. Alvarez, L. C. Chamon, D. Pereira, M. N. Rao, E. S. Rossi, Jr., L. R. Gasques, M. A. E. Santo, R. M. Anjos, J. Lubian, P. R. S. Gomes, C. Muri, B. V. Carlson, S. Kailas, A. Chatterjee, P. Singh, A. Shrivastava, K. Mahata, and S. Santra, Nucl. Phys. **A679**, 287 (2001).
[23] M. Dasgupta, D. J. Hinde, N. Rowley, and A. M. Stefanini, Annu. Rev. Nucl. Part. Sci. **48**, 401 (1998).
[24] H. Timmers, J. R. Leigh, M. Dasgupta, D. J. Hinde, R. C. Lemmon, J. C. Mein, C. R. Morton, J. O. Newton, and N. Rowley, Nucl. Phys. **A584**, 190 (1995).
[25] S. Santra, A. K. Mohanty, and P. Singh, Phys. Rev. C **60**, 024610 (1999).
[26] S. V. S. Sastry and S. Santra, Pramana **54**, 813 (2000).
[27] K. Hagino, N. Takigawa, M. Dasgupta, D. J. Hinde, and J. R. Leigh, Phys. Rev. Lett. **79**, 2014 (1997).
[28] J. Raynal, Phys. Rev. C **23**, 2571 (1981).
[29] W. T. Wagner, G. M. Crawley, and G. R. Hammerstein, Phys. Rev. C **11**, 486 (1975).